A Semi-Analytical Model Of High Permittivity Dielectric Ring Resonators for Magnetic Resonance Imaging

Marine A.C. Moussu, Marine A.C. Moussu, Redha Abdeddaim, Marc A. Dubois, Elodie Georget, Andrew G Webb, Elizaveta Nenasheva, Pavel Belov, Stanislav Glybovski, Luisa Ciobanu, et al.

A Semi-Analytical Model Of High Permittivity Dielectric Ring Resonators for Magnetic Resonance Imaging

Marine A.C. Moussu, Redha Abdeddaim, Marc Dubois, Elodie Georget, Andrew G. Webb, *Member, IEEE,* Elizaveta Nenasheva, Pavel Belov, *Member, IEEE,* Stanislav Glybovski, *Member, IEEE,* Luisa Ciobanu, and Stefan Enoch

***Abstract*—Magnetic Resonance Imaging (MRI) is an imaging technique exploiting the magnetic resonance of specific nuclear spins, like protons. In this paper, MRI probes based on dielectric ring resonators are investigated from a theoretical point of view. We take advantage of the high-permittivity and low-losses properties of the ceramic material used for manufacturing these probes for microscopy applications. Magnetic Resonance Microscopy (MRM) aims at imaging tiny samples with a sufficient resolution to distinguish small details. In this framework, compact resonators, called volume probes, contain the investigated sample and are used for both signal transmission and reception. The new developed semi-analytical model enables estimation of the frequency of the first transverse electric mode of a cylindrical resonator. It also provides a method to compute the corresponding magnetic field distribution, the dielectric losses contributions from the probe and the sample, and Signal-to-Noise Ratio (SNR). The proposed approach aims at providing design guidelines for dielectric probes.**

***Index Terms*—Dielectric Resonators, Magnetic Resonance Microscopy, Signal-to-Noise Ratio, Transverse Electric Mode**

I. Introduction

MAGNETIC Resonance Microscopy (MRM) is an imaging technique which uses the principles of magnetic resonance imaging (MRI) to produce images with a spatial resolution of less than 100 microns on at least one of the three dimensions [1]. Typical sample sizes are several millimeters or less, which places high demands on achieving the optimum Signal-to-Noise Ratio (SNR). For these reasons, MRM is usually performed using magnets with static field B_0 of more than 7 T and up to 22 T, which is currently the strongest available magnet for imaging [1]. At such ultra high magnetic field, the reference probe for volume imaging is often a solenoid, with the diameter closely matching that of the sample. The solenoid produces a large, homogeneous radiofrequency (RF) field B_1 used for excitation, but also a high electric field which can produce heating due to resistive losses in conductive samples [2]. Researchers have recently introduced configurations based on ceramic dielectric resonators to reduce the noise contribution due to the electric field in the sample [3], [4], [5].
These resonators have been successfully ntroduced in microwave engineering. They are used to significantly reduce the size of microwave circuits, especially in the evergrowing field of telecommunications [6]. They are exploited as antennas (TE mode with high quality factor) [7], [8], [9] and filters (Hybrid Electric and Magnetic (HEM) mode with low Q-factor) [10], [9], [11]. Electron Paramagnetic Resonance (EPR) is another application of such resonators to concentrate the magnetic field into a specific region [3].

In MRM, to compete with the solenoid coil, the first transverse electric mode of a cylindrical dielectric cavity, the so-called $TE_{01\delta}$ is employed as it has a maximum axial magnetic field in its center together with a minimum electric field [6]. Fig. 1 describes the placement of this probe within the bore of an MRI magnet. In this position, the orthogonality of B_1 and B_0 needed for spins excitation and signal detection, is guaranteed by the axial direction of the main B_1 component related to this mode. Several prototypes of such eramic rings were experimentally compared to a commercial reference probe and provided equivalent or higher SNR [4], [5].

While the theoretical model for solenoid coils used as Magnetic Resonance (MR) probes has been well developed [12], [13], no detailed theoretical model was so far proposed

Marine A.C. Moussu is with Multiwave Imaging, 13013, Marseille, France and Aix Marseille Univ, Centre National de la Recherche Scientifique (CNRS), Centrale Marseille, Institut Fresnel, 13013, Marseille, France (e-mail: marine.moussu@fresnel.fr).

Redha Abdeddaim is with Aix Marseille Univ, CNRS, Centrale Marseille, Institut Fresnel, 13013, Marseille, France (e-mail: redha.abdeddaim@fresnel.fr).

Stefan Enoch is with Aix Marseille Univ, CNRS, Centrale Marseille, Institut Fresnel, Institut Marseille Imaging, 13013, Marseille, France (e-mail: stefan.enoch@fresnel.fr).

Marc Dubois is with Aix Marseille Univ, CNRS, Center for Magnetic Resonance in Biology and Medicine, 13005, Marseille, France and Aix Marseille Univ, CNRS, Centrale Marseille, Institut Fresnel, 13013, Marseille, France (e-mail: marc.dubois@fresnel.fr)

Elodie Georget is with Multiwave Imaging, 13013, Marseille, France (e-mail: elodie@multiwaveimaging.com).

Andrew G. Webb is with Department of Radiology, C.J. Gorter Center for High Field MRI, Leiden University Medical Center, 2333 ZA Leiden, The Netherlands (e-mail: A.Webb@lumc.nl).

Elizaveta Nenasheva is with Ceramics Co. Ltd., Saint-Petersburg 194223, Russia (e-mail: liza@ceramics.sp.ru).

Pavel Belov and Stanislav Glybovski are with ITMO University 197101, Saint. Petersburg, Russia (e-mails: belov@metalab.ifmo.ru, s.glybovski@metalab.ifmo.ru).

Luisa Ciobanu is with Commissariat à l'Energie Atomique et aux Energies Alternatives (CEA), Direction de la Recherche Fondamentale (DRF), Institut des Sciences du Vivant Frédéric-Joliot (JOLIOT), NeuroSpin, Université Paris-Saclay, Gif-sur-Yvette, France (e-mail: luisa.ciobanu@cea.fr).

for MR probes based on dielectric ring resonators. However, such a model could give the possibility of adjusting ceramics properties and resonator dimensions to design dielectric probes with maximum efficiency for a given sample.

The resonant frequencies, the field distribution and the quality factor of cylindrical dielectric resonators have been investigated for many years. From the literature, two types of approaches can be distinguished:

- Accurate and rigorous methods with high computational cost, allowing to determine both the resonant frequencies and the field distribution while considering complex configurations (shielded dielectric resonator, in a waveguide, isolated, on a substrate, and so on). Among others, these methods are the surface integral equation solved with the method of moments [14], the perturbational approach with asymptotic expansions [15], [16], the finite elements method [17] and the mode matching methods for solving the corresponding boundary value problem [11], [10], [6].
- Simplified models that provide an approximated estimation of the characteristics of a given mode, most of the time the first TE or TM mode:
  - Perfect Magnetic Conductor walls are assumed at the lateral boundaries of the resonator like in [18], [8], or the second-order Cohn's model for both isolated or shielded resonator [19];
  - The tangential field continuity is ensured at the resonator's lateral boundaries and/or at its terminal ends, like in the Itoh and Rudoka's model [20].

More recently, such an approximated theoretical model of cylindrical dielectric resonators first TE mode, based on the lumped-elements equivalent circuit approach, has been developed for EPR applications [21], [22].

In this paper, we present a model describing the excited field distribution of the ceramic probe: the first transverse electric mode ($TE_{01\delta}$) of a cylindrical, high-permittivity resonator. Our model is described as "semi-analytical" in the following, because it is based on the analytical expression of the electromagnetic (EM) field but requires the numerical solving of a set of equations to estimate the wavenumbers describing the field. In this approach, the ceramic probe consists in a dielectric ring (green in Fig. 1) containing a sample medium (light blue). A formula is proposed for the resonant frequency of this system, which is approximated to that of a filled disk, assuming that the effect of the hole is negligible. The field distribution is computed from the description of the electromagnetic (EM) field in the sample, within the dielectric ring, and around it. This semi-analytical approach is then used to derive a quantitative estimation of the reachable SNR performance of ceramic probes. The practical example used is designed for a Larmor frequency f_L = 730 MHz and previously presented experimentally in Reference [23], with a ring of given height of 10 mm, outer diameter 18 mm and inner diameter 5.6 mm, and dielectric material of relative permittivity 536 and loss tangent $8{\cdot}10^{-4}$.

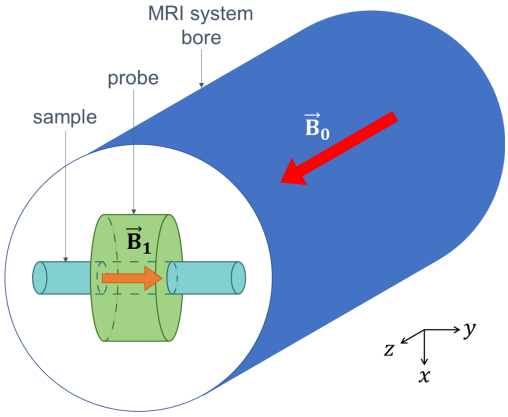

Figure 1. Configuration of the setup: the axis of the dielectric probe is perpendicular to the MRI system axis.

II. $TE_{01\delta}$ MODE DESCRIPTION

The principle of the dielectric probe presented in this paper relies on the excitation of its first TE mode, which magnetic field distribution in the sample is similar to that of the solenoid coil while its electric field spatial behavior is radically different. In this part, we provide semi-analytic tools to describe the EM field of the exploited $TE_{01\delta}$, in order to, in section III, derive an expression for the dielectric losses induced by this probe.

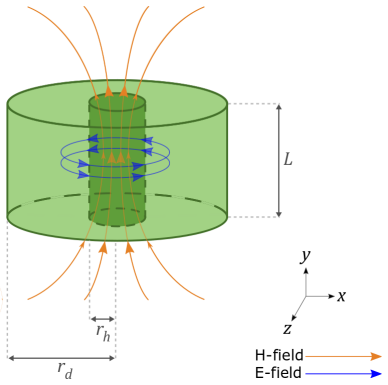

Figure 2. $TE_{01\delta}$ mode of a ring resonator (schematic field lines), notations and coordinates system

The ceramic probe is a cylindrical ring resonator, as represented in Fig. 2, made of a material with a very high-permittivity (to ensure a good mode confinement), low-loss (to lower the probe intrinsic losses) dielectric material surrounded by a low-permittivity medium (air). Due to the high permittivity contrast between the background material and the resonator, the electromagnetic field distribution at resonance can be assumed to be mainly confined within the resonator. The reflection coefficient between air and high-permittivity dielectric material, equal to $\left(\sqrt{\epsilon_r}-1\right)/\left(\sqrt{\epsilon_r}+1\right)$ [24], is indeed close to 1. In this context, first analytical approaches of cylindrical dielectric resonators are based on the assumption of Perfect Magnetic Conductor (PMC) boundary conditions at the lateral frontiers of the structure [18], [25].
The resonant modes of such a cylindrical structure are clas-

sified following the same notations as for metallic cavities, except that the integer numbers quantifying the wavenumbers are replaced by non-integer numbers [26]. In cylindrical coordinates (ρ, θ, y), a transverse electric mode is fully described by its axial magnetic component H_y whose generic expression within the cavity is given for a disk resonator in Eq. (1) [27], [25].

$$\mathrm{H}_y = A\cos(n\theta+\phi)\,\mathrm{J}_n(\alpha\rho)\cos(\beta y+\psi) \tag{1}$$

The mode nomenclature for a dielectric cavity is of the form $\mathrm{TE}_{nm(p+\delta)}$ in reference to metallic cavities, where n is the integer number for the field angular variations, m an integer number describing the order of radial field variations, and $p+\delta$ (p integer, δ a number between 0 and 1) quantifies the product βL of the axial wavenumber β with the resonator height L. The first transverse electric mode of a cylindrical resonator, named $\mathrm{TE}_{01\delta}$, corresponds to an electromagnetic field with a cylindrical symmetry with respect to the resonator axis (no angular variation). In the center, the electric field $\mathbf{E}$ decreases to zero while the magnetic field $\mathbf{H}$ is maximum and mainly parallel to the resonator axis [6], [3], two features of great interest for an MRM probe.

A. Disk resonator frequency estimation

In this section, several approaches for estimating the $\mathrm{TE}_{01\delta}$ mode eigenfrequency of a cylindrical dielectric resonator, neglecting dielectric losses within the resonator material, are presented. In the microwave resonators literature, one can found a wide variety of methods developed to estimate the $\mathrm{TE}_{01\delta}$ mode frequency with different levels of accuracy. A first starting point is to approximate the value of the resonant frequency of the isolated resonator by Eq. (2) [6], with f_{MHz} the frequency (in megaherz), ϵ_r the relative permittivity, r_d the disk radius and L the disk height. This equation was deduced by fitting simulation data, and despite a limited domain of validity (radius over height ratio: $0.5 < r_\mathrm{d}/L < 2$ and relative permittivity: $30 < \epsilon_\mathrm{r} < 50$) where accuracy is ensured around 2%, it can be used to give a reasonable approximation for any high permittivity disk resonator.

$$f_{\mathrm{MHz}} = \frac{3400}{\sqrt{\epsilon_\mathrm{r}} r_{\mathrm{d,cm}}}\left(\frac{r_\mathrm{d}}{L}+3.45\right) \tag{2}$$

To extend the validity range of the estimation in terms of resonator parameters, the simplest approach in terms of computational cost consists in considering the cylindrical dielectric resonator as a shortened section of an infinite dielectric waveguide with no field leakages on its lateral boundaries. The radial wavenumber α is the same as for a circular waveguide with Perfect Magnetic Conductor (PMC) lateral boundaries $\alpha = \frac{x_{01}}{r_d}$ where x_{01} is the first zero of the Bessel function of the first kind, of order zero, and r_d the cylinder radius [19]. The axial wavenumbers ($\beta^2 = \epsilon_r k_0^2 - \alpha^2$ within the dielectric and $\gamma^2 = k_0^2 - \alpha^2$ outside, k_0 the wavenumber in vacuum) are related to the resonant frequency $f_{\mathrm{cutoff}} = k_0 c_0/(2\pi)$ (with c_0 the speed of light in vacuum) through the transcendental equation $\beta\tan\left(\frac{\beta L}{2}\right) = \gamma$, as covered in Ref. [25] under the description of the cut-off waveguide approach. This method usually underestimates the resonant frequency of the first TE mode [20].

An empirical formula was also proposed in [28], [29] to provide a reliable estimation of the resonant frequency $f_{\mathrm{empirical}}$ (Eq. (3)).

$$f_{\mathrm{empirical}} = \frac{2.9c}{2\pi r_\mathrm{d}\epsilon_\mathrm{r}^{0.46}}\left[0.7+0.3\frac{r_\mathrm{d}}{L}-0.03\left(\frac{r_\mathrm{d}}{L}\right)^2\right] \tag{3}$$

Similar to the method presented in [30], the resonant frequency f_{res} is estimated as the average of the two last approaches, as expressed in Eq. (4).

$$f_{\mathrm{res}} = \frac{1}{2}\left(f_{\mathrm{empirical}} + f_{\mathrm{cutoff}}\right) \tag{4}$$

For comparison to a reference method, the gold-standard resonance frequency of the same dielectric disk $f_{\mathrm{ref,disk}}$ is calculated using the numerical simulations with the eigenmode solver of CST Microwave Studio. The reliability of the proposed method that provides the approximated value f_{res} (Eq. (4)), was investigated by comparison with the numerical simulations, for discretized values among the following parameter ranges:

- Relative permittivity ϵ_r varying from 200 to 1000;
- Disk height L from 5 to 20 mm;
- Disk radius r_d from 5 to 15 mm.

In Fig. 3, the resonant frequency is calculated with Eq. (4) for a continuous range of heights, and discrete values of the disk radius and relative permittivity. The comparison of these results to the gold standard is quantified through the relative error defined in Eq. (5). For the considered ranges of parameters, the proposed estimation f_{res} has a maximum relative error of 5.3 %, all other cases have an error less than 5 % and more than half are below 3 %, which validates this approach.

$$\mathcal{E}_{f,\mathrm{ref}} = \frac{|f_{\mathrm{res}} - f_{\mathrm{ref,disk}}|}{f_{\mathrm{ref,disk}}} \times 100 \tag{5}$$

The MRM ceramic probe studied is described as a high-permittivity ($\epsilon_d = \epsilon_0\epsilon_r$) ring resonator (outer radius r_d, inner radius r_h, height L), filled with a lower-permittivity (ϵ_s) material representing the sample (cylinder of radius r_h and height L). Such a structure has resonant modes that can be described in the same manner as for a disk of same high-permittivity ϵ_r than the probe [17]. In the particular case of the first TE mode, equating the field distribution of the probe and the disk resonators is even a reasonable assumption. Indeed, the first TE mode features are affected in proportion to the electric and magnetic energies stored in the involved volume [31], which coarsely depends on the quantity $\Delta\epsilon \times \mathrm{V}_{\mathrm{samp}}$ ($\Delta\epsilon = \epsilon_\mathrm{s} - \epsilon_\mathrm{d}$, $\mathrm{V}_{\mathrm{samp}}$ the sample volume). In particular, in first approximation, the mode frequency varies from the value f_{disk} for the disk to f_{probe} for the probe according to Eq. (6) from [31].

$$\frac{f_{\mathrm{probe}} - f_{\mathrm{disk}}}{f_{\mathrm{disk}}} \approx \frac{-\iiint_{V_{\mathrm{samp}}} \Delta\epsilon |\overrightarrow{E}_{\mathrm{disk}}|^2 d^3\mathbf{r}}{\iiint_{V_{\mathrm{ring}}\cup V_{\mathrm{samp}}} \left(\epsilon_\mathrm{d}|\overrightarrow{E}_{\mathrm{disk}}|^2 + \mu_0|\overrightarrow{H}_{\mathrm{disk}}|^2\right) d^3\mathbf{r}} \tag{6}$$

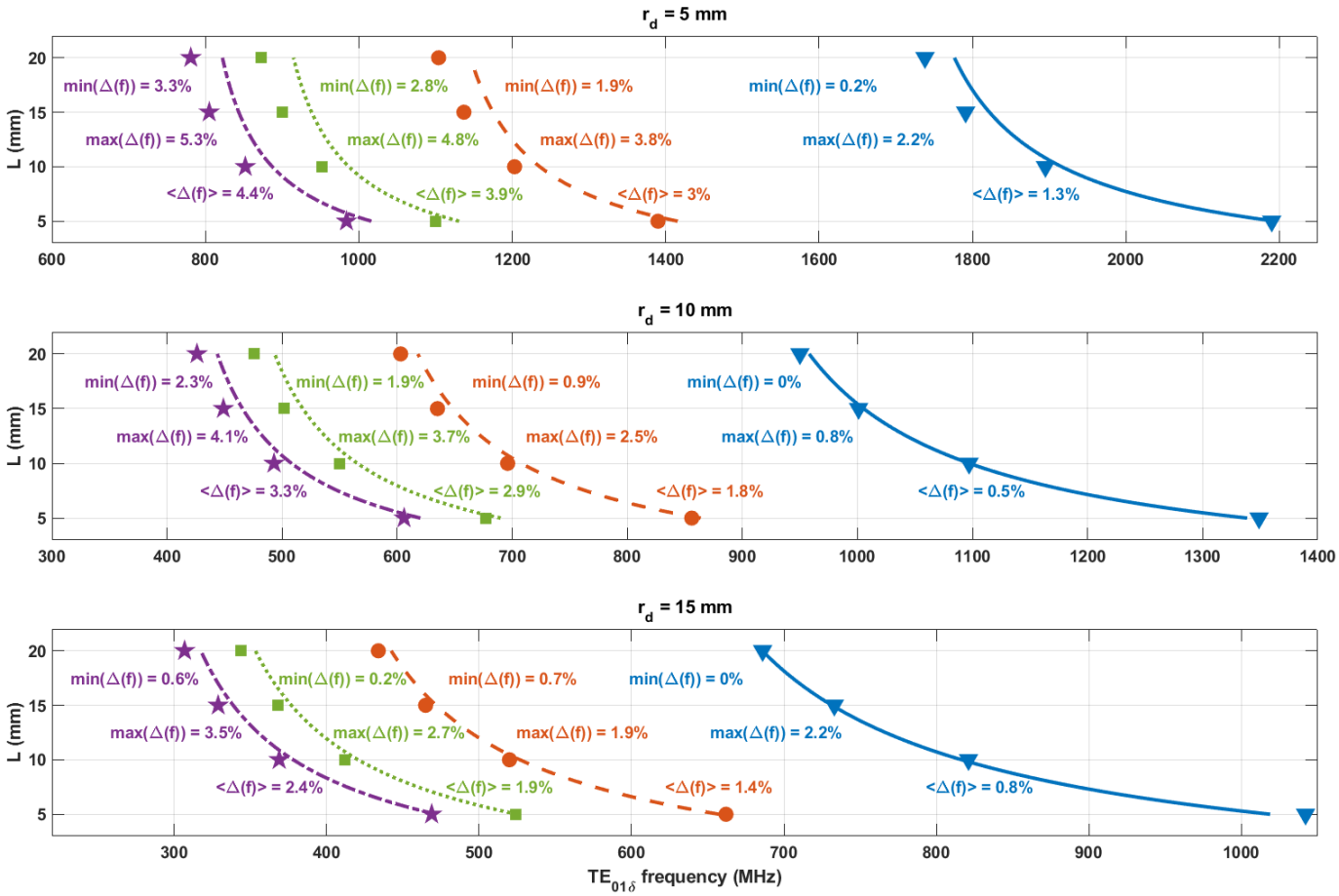

Figure 3. Comparison between numerical simulations and semi-analytical method (Eq. (4)) of $TE_{01\delta}$ eigenmode frequency estimation as a function of the disk height (L), radius (r_d) and permittivity (blue: 200, orange: 500, green: 800, purple: 1000). Lines represent the results from the semi-analytical method proposed in this paper (f_{res}, Eq. (4)), and markers represent CST results. For each curve, the maximum, minimum and averaged value of the relative error Δ(f) are indicated.

From this expression, it can be seen that the TE mode frequency is affected by the permittivity contrast between the dielectric ring and the sample. More precisely, as the sample has a lower permittivity than the ring material, the permittivity contrast $\Delta\epsilon$ is negative and the frequency shift is therefore positive. In the framework of MRI, it means that the working frequency of the dielectric probe depends on the sample, and therefore must be adjusted on demand at the desired nucleus Larmor frequency. To do so, several methods have been developed, including coupling with copper foils [4] or with a second dielectric resonator [5], and thermostating the probe to change its permittivity as it depends on the temperature [23]. On the other side, the sample volume V_{samp} is in the region where the E-field distribution is minimum, as it vanishes in the center of the structure. In this work, we assume the same field distribution for the system $\{\text{ring} + \text{sample}\}$ as for the disk when estimating the mode frequency in this section, and the SNR factor in section IV. This hypothesis is valid while the permittivity contrast, together with the sample over disk radii ratio $r_{\text{h}}/r_{\text{d}}$, have reasonable values, as presented in the following.

Figure 4 illustrates the influence of the sample on the $TE_{01\delta}$ mode frequency in the case of a probe with outer radius r_{d} = 10 mm, height L = 10 mm, varying permittivity ϵ_{r} and sample properties r_{h} and $\epsilon_{\text{r,samp}}$. The frequencies used in this part are estimated with the Eigenmode solver of CST Studio. For three values of relative permittivity of the dielectric material constituting the probe ϵ_{r} (200, 500 and 800), the relative variation $\mathcal{E}_{f,\text{disk/probe}}$ between the disk frequency $f_{\text{ref,disk}}$ and that of the probe $f_{\text{ref,probe}}$ is estimated (Eq. 7).

$$\mathcal{E}_{f,\text{disk/probe}} = \frac{|f_{\text{ref,probe}} - f_{\text{ref,disk}}|}{f_{\text{ref,disk}}} \times 100 \qquad (7)$$

The sample permittivity range covers covers a wide variety of biological samples. As expected from Eq. (6), the relative variation is a linear function of the sample permittivity. A general observation from this figure is that the radii ratio $r_{\text{h}}/r_{\text{d}}$ has a dominant influence over the frequency variation, all the more than the relative permittivity of the probe ring is high. Indeed, while the sample radius r_{h} is smaller than 0.4 times the probe radius r_{d}, the frequency shift due to the sample is inferior to 5% for all permittivities considered.

B. Field distribution

As for the resonance frequency of the $TE_{01\delta}$ mode of a disk resonator, several approaches have been proposed to estimate

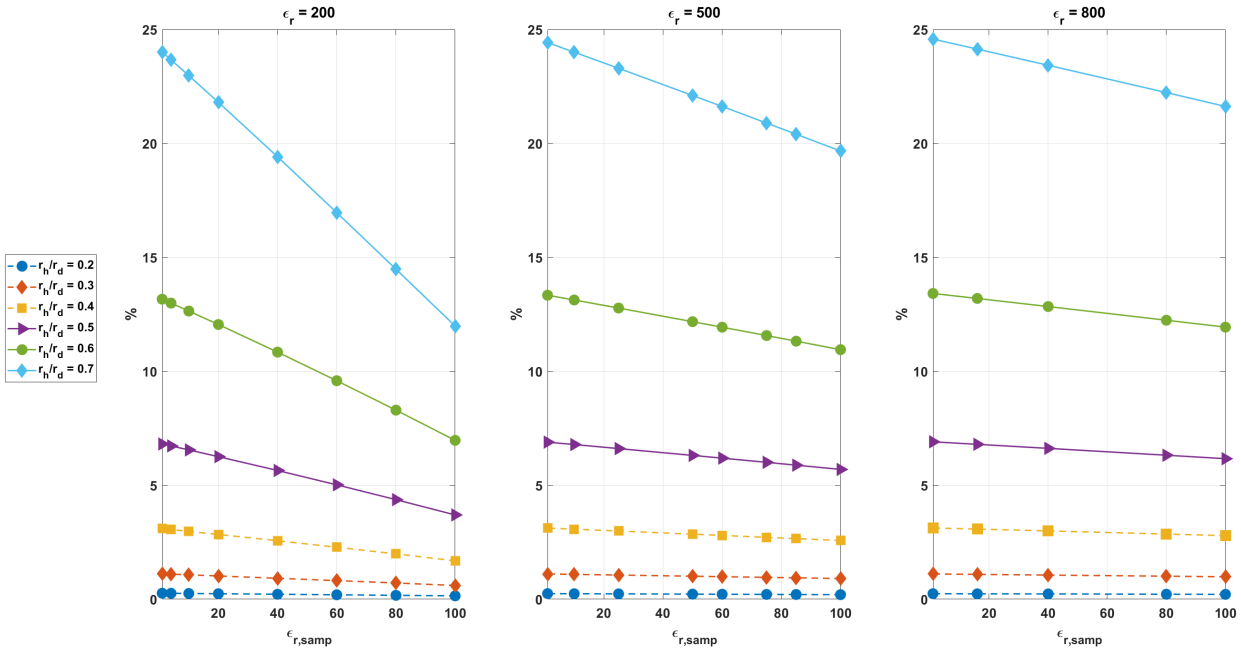

Figure 4. Quantification of the $TE_{01\delta}$ mode frequency shift between the disk resonator and the dielectric probe (for both, numerical simulations results with CST Eigenmode Solver). The probe ring has its relative permittivity equal to 200 (left), 500 (center) and 800 (right). The frequency variation is plotted as a function of the sample permittivity and for several discrete values of the radii ratio. Curves in dashed lines correspond to systematic frequency shift inferior to 5%.

the corresponding EM-field distribution: rigorous numerical methods with heavy computation cost, and simplified models which the error depends on the rudeness of the hypothesis [6]. Among the second category, the approach proposed by Sheen [32] is an interesting trade-off between accurary of the field distribution and simplicity of implementation. In [32], it is presented for the parallel-plate dielectric disk, meaning that the disk is placed between two conducting plates. In the following, we propose a similar method for the parallel-plate dielectric ring. In both methods, the field distribution is estimated for lossless dielectric materials.

This method, for computing the field distribution of the ring resonator $TE_{01\delta}$ mode, is based on the part-by-part subdivision of the space surrounding the resonator. These regions are indexed from I $\rightarrow$ IX and are represented in Fig. 5. Each of these regions corresponds to a homogeneous relative permittivity distribution: region I represents the sample, region II the ceramic material constitutive of the probe, and regions III $\rightarrow$ IX the surrounding media which are here taken as air ($\epsilon_{r,\mathrm{III}\rightarrow\mathrm{IX}} = 1$).

The next step consists in analytically describing the mode in a cylindrical coordinate system (ρ, θ, y). According to its specifications, this TE mode has a cylindrical symmetry, which means that only three field components are nonzero [6], [27]: H_y, E_θ and H_ρ. Solving the Helmholtz's equation in cylindrical coordinates leads to the following field expression properties [6]:

- the radial variation involves linear combinations of the Bessel functions J and Y or the modified Bessel function K, with the radial wavenumber $k_{\rho,i}$ in region i;

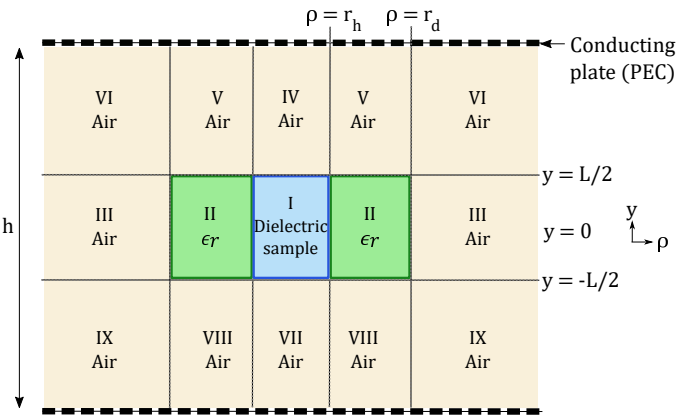

Figure 5. Part by part space subdivision for field estimation.

- the axial variation is expressed with a sinusoidal function and the axial wavenumber $k_{y,i}$ in region i.

The wavenumber components in region i are related to the total wavenumber in vacuum k_0 by Eq. (8).

$$k_{\rho,i}^2 + k_{y,i}^2 = \epsilon_{r,i} k_0^2 \tag{8}$$

The model is based on the assumption of purely propagative EM field in the probe, with real wavenumbers $k_{\rho,II} = \alpha_{\mathrm{II}}$ and $k_{y,II} = \beta$ in the dielectric ring, that imposes the mode. Leakages through the resonator boundaries are also considered. In the sample (region I), the axial wavenumber is real by field continuity with the ring, but the radial wavenumber α_{I} is defined by the relative values of k_0 and $k_{\rho,\mathrm{II}}$. Outside the probe, the field is either propagative either evanescent in

one or two directions, y and ρ. For evanescent contributions, the corresponding wavenumber is imaginary: $k_{\rho,\mathrm{i}} = j\nu_\mathrm{i}$ and $k_{\mathrm{y,i}} = j\gamma_\mathrm{i}$.

The field expressions for H_y and E_θ are given in Eqs. (9) and (10), respectively. The third component H_ρ can be derived from H_y and its expression is provided in regions I, IV and VII (Eq. (11)) only since the others are unused in the following for calculations.

$$\begin{aligned}
\mathrm{H}_y^{\mathrm{I}} &= a_\mathrm{I}\mathrm{J}_0\left(\alpha_\mathrm{I}\rho\right)\cos\left(\beta y\right)\\
\mathrm{H}_y^{\mathrm{II}} &= a_\mathrm{II}\left[\mathrm{J}_0\left(\alpha_\mathrm{II}\rho\right)+\xi\mathrm{Y}_0\left(\alpha_\mathrm{II}\rho\right)\right]\cos\left(\beta y\right)\\
\mathrm{H}_y^{\mathrm{III}} &= a_\mathrm{III}\mathrm{K}_0\left(\nu_\mathrm{III}\rho\right)\cos\left(\beta y\right)\\
\mathrm{H}_y^{\mathrm{IV}} &= a_\mathrm{IV}\mathrm{J}_0\left(\alpha_\mathrm{I}\rho\right)\sinh\left[\gamma\left(y-y_\mathrm{lim}\right)\right]\\
\mathrm{H}_y^{\mathrm{V}} &= a_\mathrm{V}\left[\mathrm{J}_0\left(\alpha_\mathrm{II}\rho\right)+\xi\mathrm{Y}_0\left(\alpha_\mathrm{II}\rho\right)\right]\sinh\left[\gamma\left(y-y_\mathrm{lim}\right)\right]\\
\mathrm{H}_y^{\mathrm{VI}} &= a_\mathrm{VI}\mathrm{K}_0\left(\nu_\mathrm{III}\rho\right)\sinh\left[\gamma\left(y-y_\mathrm{lim}\right)\right]\\
\mathrm{H}_y^{\mathrm{VII}} &= a_\mathrm{VII}\mathrm{J}_0\left(\alpha_\mathrm{I}\rho\right)\sinh\left[-\gamma\left(y+y_\mathrm{lim}\right)\right]\\
\mathrm{H}_y^{\mathrm{VIII}} &= a_\mathrm{VIII}\left[\mathrm{J}_0\left(\alpha_\mathrm{II}\rho\right)+\xi\mathrm{Y}_0\left(\alpha_\mathrm{II}\rho\right)\right]\sinh\left[-\gamma\left(y+y_\mathrm{lim}\right)\right]\\
\mathrm{H}_y^{\mathrm{IX}} &= a_\mathrm{IX}\mathrm{K}_0\left(\nu_\mathrm{III}\rho\right)\sinh\left[-\gamma\left(y+y_\mathrm{lim}\right)\right]
\end{aligned} \tag{9}$$

$$\begin{aligned}
\mathrm{E}_\theta^{\mathrm{I}} &= a_\mathrm{I}\frac{j\omega\mu_0}{\alpha_\mathrm{I}}\mathrm{J}_1\left(\alpha_\mathrm{I}\rho\right)\cos\left(\beta y\right)\\
\mathrm{E}_\theta^{\mathrm{II}} &= a_\mathrm{II}\frac{j\omega\mu_0}{\alpha_\mathrm{II}}\left[\mathrm{J}_1\left(\alpha_\mathrm{II}\rho\right)+\xi\mathrm{Y}_1\left(\alpha_\mathrm{II}\rho\right)\right]\cos\left(\beta y\right)\\
\mathrm{E}_\theta^{\mathrm{III}} &= -a_\mathrm{III}\frac{j\omega\mu_0}{\nu_\mathrm{III}}\mathrm{K}_1\left(\nu_\mathrm{III}\rho\right)\cos\left(\beta y\right)\\
\mathrm{E}_\theta^{\mathrm{IV}} &= a_\mathrm{IV}\frac{j\omega\mu_0}{\alpha_\mathrm{I}}\mathrm{J}_1\left(\alpha_\mathrm{I}\rho\right)\sinh\left[\gamma\left(y-y_\mathrm{lim}\right)\right]\\
\mathrm{E}_\theta^{\mathrm{V}} &= a_\mathrm{V}\frac{j\omega\mu_0}{\alpha_\mathrm{II}}\left[\mathrm{J}_1\left(\alpha_\mathrm{II}\rho\right)+\xi\mathrm{Y}_1\left(\alpha_\mathrm{II}\rho\right)\right]\\
&\quad\times\sinh\left[\gamma\left(y-y_\mathrm{lim}\right)\right]\\
\mathrm{E}_\theta^{\mathrm{VI}} &= -a_\mathrm{VI}\frac{j\omega\mu_0}{\nu_\mathrm{III}}\mathrm{K}_1\left(\nu_\mathrm{III}\rho\right)\sinh\left[\gamma\left(y-y_\mathrm{lim}\right)\right]\\
\mathrm{E}_\theta^{\mathrm{VII}} &= a_\mathrm{VII}\frac{j\omega\mu_0}{\alpha_\mathrm{I}}\mathrm{J}_1\left(\alpha_\mathrm{I}\rho\right)\sinh\left[-\gamma\left(y+y_\mathrm{lim}\right)\right]\\
\mathrm{E}_\theta^{\mathrm{VIII}} &= a_\mathrm{VIII}\frac{j\omega\mu_0}{\alpha_\mathrm{II}}\left[\mathrm{J}_1\left(\alpha_\mathrm{II}\rho\right)+\xi\mathrm{Y}_1\left(\alpha_\mathrm{II}\rho\right)\right]\\
&\quad\times\sinh\left[-\gamma\left(y+y_\mathrm{lim}\right)\right]\\
\mathrm{E}_\theta^{\mathrm{IX}} &= -a_\mathrm{IX}\frac{j\omega\mu_0}{\nu_\mathrm{III}}\mathrm{K}_1\left(\nu_\mathrm{III}\rho\right)\sinh\left[-\gamma\left(y+y_\mathrm{lim}\right)\right]
\end{aligned} \tag{10}$$

$$\begin{aligned}
\mathrm{H}_\rho^{\mathrm{I}} &= -a_\mathrm{I}\frac{\beta}{\alpha_\mathrm{I}}\mathrm{J}_1\left(\alpha_\mathrm{I}\rho\right)\sin\left(\beta y\right)\\
\mathrm{H}_\rho^{\mathrm{IV}} &= a_\mathrm{IV}\frac{\gamma}{\alpha_\mathrm{I}}\mathrm{J}_1\left(\alpha_\mathrm{I}\rho\right)\cosh\left[\gamma\left(y-y_\mathrm{lim}\right)\right]\\
\mathrm{H}_\rho^{\mathrm{VII}} &= -a_\mathrm{VII}\frac{\gamma}{\alpha_\mathrm{I}}\mathrm{J}_1\left(\alpha_\mathrm{I}\rho\right)\cosh\left[-\gamma\left(y+y_\mathrm{lim}\right)\right]
\end{aligned} \tag{11}$$

The axial wavenumber γ is the same in absolute value be it for $y > \frac{L}{2}$ (regions IV, V and VI) or $y < -\frac{L}{2}$ (regions VIII, IX and X) since the resonator is at equal distance from the conducting plates. The E-field cancellation on the PEC boundaries gives $y_\mathrm{lim} = \frac{h}{2}$. In the following examples, h is taken equal to 11 cm, that corresponds to the shielded bore diameter of the MRI device used in [23].

The wavenumber components are determined using the tangential field continuity conditions in (12): $\mathrm{H}_y^{\mathrm{I}} = \mathrm{H}_y^{\mathrm{II}}$ and $\mathrm{E}_\theta^{\mathrm{I}} = \mathrm{E}_\theta^{\mathrm{II}}$ at $\rho = r_\mathrm{h}$, $\mathrm{H}_y^{\mathrm{II}} = \mathrm{H}_y^{\mathrm{III}}$ and $\mathrm{E}_\theta^{\mathrm{II}} = \mathrm{E}_\theta^{\mathrm{III}}$ at $\rho = r_\mathrm{d}$, and $\mathrm{E}_\theta^{\mathrm{I}} = \mathrm{E}_\theta^{\mathrm{IV}}$ and $\mathrm{H}_y^{\mathrm{I}} = \mathrm{H}_y^{\mathrm{IV}}$ at $y = \pm\frac{L}{2}$. The latest is written only at $y = +\frac{L}{2}$ as it gives the same equation than in $y = -\frac{L}{2}$.

$$\begin{aligned}
a_\mathrm{I}\mathrm{J}_0\left(\alpha_\mathrm{I}r_\mathrm{h}\right) &= a_\mathrm{II}\left[\mathrm{J}_0(\alpha_\mathrm{II}r_\mathrm{h})+\xi\mathrm{Y}_0(\alpha_\mathrm{II}r_\mathrm{h})\right]\\
\frac{a_\mathrm{I}}{\alpha_\mathrm{I}}\mathrm{J}_1\left(\alpha_\mathrm{I}r_\mathrm{h}\right) &= \frac{a_\mathrm{II}}{\alpha_\mathrm{II}}\left[\mathrm{J}_1(\alpha_\mathrm{II}r_\mathrm{h})+\xi\mathrm{Y}_1(\alpha_\mathrm{II}r_\mathrm{h})\right]\\
a_\mathrm{II}\left[\mathrm{J}_0(\alpha_\mathrm{II}r_\mathrm{d})+\xi\mathrm{Y}_0(\alpha_\mathrm{II}r_\mathrm{d})\right] &= a_\mathrm{III}\mathrm{K}_0\left(\nu_\mathrm{III}r_\mathrm{d}\right)\\
\frac{a_\mathrm{II}}{\alpha_\mathrm{II}}\left[\mathrm{J}_1(\alpha_\mathrm{II}r_\mathrm{d})+\xi\mathrm{Y}_1(\alpha_\mathrm{II}r_\mathrm{d})\right] &= -\frac{a_\mathrm{III}}{\nu_\mathrm{III}}\mathrm{K}_1\left(\nu_\mathrm{III}r_\mathrm{d}\right)\\
a_\mathrm{I}\cos\left(\frac{\beta L}{2}\right) &= a_\mathrm{IV}\sinh\left(\gamma\frac{L-h}{2}\right)\\
-a_\mathrm{I}\beta\sin\left(\frac{\beta L}{2}\right) &= a_\mathrm{IV}\gamma\cosh\left(\gamma\frac{L-h}{2}\right)
\end{aligned} \tag{12}$$

Combining the first four equations of (12) and (8) leads to the set of equations (13), which is equivalent to the eigenvalue problem of a circular dielectric waveguide as presented in [33]. This type of system of equations admits complex solutions, as demonstrated in [34]. It is numerically solved with respect to the real variable β. The solutions of this system can be graphically represented by distinct curves representing the wavenumber k_0 as a function of β. The dispersion curves of the first three modes of such waveguide are given as example in Fig. 6. The lowest frequency curve is the first order mode of the corresponding infinite dielectric waveguide and is the solution considered in the following.

$$\begin{aligned}
\frac{\mathrm{J}_1(u)}{u\mathrm{J}_0(u)} &= \frac{1}{v}\frac{\mathrm{J}_1(v)+\xi\mathrm{Y}_1(v)}{\mathrm{J}_0(v)+\xi\mathrm{Y}_0(v)}\\
-\frac{\mathrm{K}_1(x)}{x\mathrm{K}_0(x)} &= \frac{1}{\frac{r_\mathrm{d}}{r_\mathrm{h}}v}\frac{\mathrm{J}_1(\frac{r_\mathrm{d}}{r_\mathrm{h}}v)+\xi\mathrm{Y}_1(\frac{r_\mathrm{d}}{r_\mathrm{h}}v)}{\mathrm{J}_0(\frac{r_\mathrm{d}}{r_\mathrm{h}}v)+\xi\mathrm{Y}_0(\frac{r_\mathrm{d}}{r_\mathrm{h}}v)}\\
u &= r_\mathrm{h}\sqrt{\epsilon_{r,samp}k_0^2-\beta^2}\\
v &= r_\mathrm{h}\sqrt{\epsilon_r k_0^2-\beta^2}\\
x &= r_\mathrm{d}\sqrt{-k_0^2+\beta^2}\\
\xi &= \frac{u\mathrm{J}_0(u)\mathrm{J}_1(v)-v\mathrm{J}_0(v)\mathrm{J}_1(u)}{v\mathrm{Y}_0(v)\mathrm{J}_1(u)-u\mathrm{J}_0(u)\mathrm{Y}_1(v)}
\end{aligned} \tag{13}$$

Next, combining the last two equations of (12) and (8) leads to the set of equations (14), which is equivalent to the eigenvalue problem of a planar dielectric waveguide [25]. In the same manner, (14) is numerically solved with respect to β. It gives several solutions depicting the different planar waveguide modes, as illustrated by the dashed dispersion curves in Fig. 6.

$$\begin{aligned}
\beta\tan\left(\beta\frac{L}{2}\right) &= \gamma\coth\left(\gamma\frac{h-L}{2}\right)\\
\gamma &= \sqrt{\left(\epsilon_r-1\right)k_0^2-\beta^2}
\end{aligned} \tag{14}$$

The modes of the dielectric resonators are deduced from the intersection of the abovementioned two sets of solutions. The lowest β intersection point corresponds to the first order mode of the planar waveguide combined with the first order mode of the circular waveguide, that is, the $\mathrm{TE}_{01\delta}$ mode of

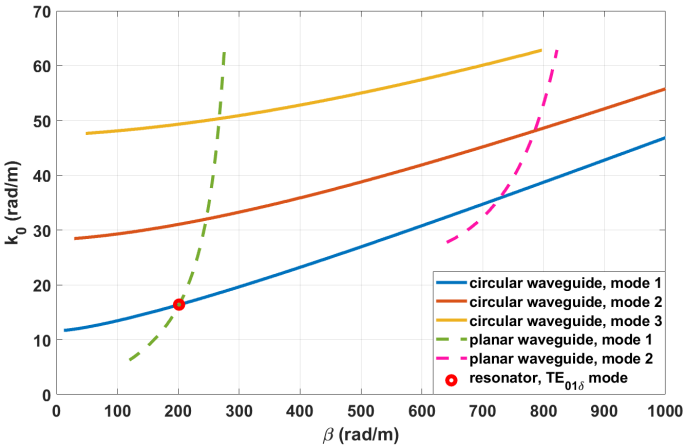

Figure 6. Dispersion curves of the infinite dielectric circular (solid lines) and planar (dashed lines) waveguides corresponding to the cylindrical resonator from Reference [23] (with $\epsilon_{\text{r,samp}} = 50$). Only the three (respectively two) first modes of the circular (resp. planar) waveguide can be seen in the considered ranges of frequencies and β values. The first TE mode of this ring resonator is shown with a red circle at the intersection point of the first waveguides modes.

the dielectric resonator, as illustrated in Fig. 6. The other wavenumber components are deduced from the β value using Eq. (8).

Fig. 7 shows examples of field maps estimated with this approach for a dielectric ring of outer radius r_{d} = 10 mm, height L = 10 mm and relative permittivity ϵ_{r} = 500, filled with a sample of varying radius r_{h} and relative permittivity $\epsilon_{\text{r,samp}}$ = 50. The smaller the ratio $r_{\text{h}}/r_{\text{d}}$, the more the magnetic field is confined within the sample with high intensity, while the region in which the electric field is minimum is only slightly affected in terms of lateral dimensions when the sample diameter increases, as can be seen on Fig. 7 (bottom line).

The validity of this approach to estimate the field distribution is compared with numerical simulations from CST Studio Eigenmode solver. In particular, it is quantified through the FieID Normalized Root Mean Squared Error FD-NRMSE expressed in Eq. (15): at each point r_n of the selected grid Ω, the relative error between the reference field component U_{ref} and the SAM field component U is computed, and the FD-NRMSE is the squared sum of all these error terms divided by the number of points of the grid $\text{N}_{\text{pts}}^{\Omega}$.

$$\text{FD-NRMSE} = \frac{1}{\text{N}_{\text{pts}}^{\Omega}} \sum_{n=1}^{\text{N}_{\text{pts}}^{\Omega}} \left(\frac{\text{U}(\mathbf{r_n}) - \text{U}_{\text{ref}}(\mathbf{r_n})}{\text{U}_{\text{ref}}(\mathbf{r_n})} \right)^2 \tag{15}$$

Fig. 8 provides quantitative values of this error. The reference field is exported from numerical simulations (CST Studio, Eigenmode Solver). The figure displays the FD-NRMSE computed in the sample along the lines of equation $y = 0$ (top graph) and $\rho = 0$. It is plotted as a function of the relative permittivity of the dielectric material of the probe. In each case, the $\text{TE}_{01\delta}$ mode of the corresponding disk resonator is adjusted to the Larmor frequency at 17.2 T (730 MHz) via its diameter, as covered in section II-A. The resonator height is kept equal to 10 mm. The FD-NRMSE never exceeds 5 %. Increasing the permittivity, which involves a higher confinement of the mode in the probe, also leads to an improvement in the accuracy of the semi-analytical method regarding the radial field distribution.

III. Power Losses Estimation

When designing a dielectric probe for MRI, one key feature that must be quantified is the proportion of input power lost during acquisition, be it in the probe itself or in the sample. This is a necessary step to estimate the noise induced by these losses. In this section, we propose a simplified approach to estimate the contributions to power losses from the probe and from the sample. This will be used in section IV to evaluate the SNR provided by a dielectric probe as a function of its geometrical and electromagnetic properties.

When an object of volume Ω and material of complex permittivity $\epsilon = \epsilon' - j\epsilon''$ (with our notations, $\epsilon' = \epsilon_0\epsilon_r \geq 0$ and $\epsilon'' = \epsilon' \tan\delta$) is immersed in an electromagnetic field, energy is dissipated in the form of heat [35].

This is caused by two phenomenon: electric conduction if the density of free electrons is non zero, and bound charges polarization [24]. In our notation, the material loss tangent includes both contributions: $\tan\delta = \tan\delta_{\text{—cond}} + \tan\delta_{\text{—polar}}$. Power losses in the object are expressed as the integral over its volume Ω, of the power losses density p, as in Eq. (16) [35].

$$\begin{aligned} P_{\text{loss}} &= \int_{\Omega} p(\mathbf{r})\, \mathrm{d}^3\mathbf{r} \\ p &= \frac{1}{2}\omega\epsilon''|\overrightarrow{\mathrm{E}}|^2 \end{aligned} \tag{16}$$

High-permittivity materials that can be used to build dielectric probe are ceramics, as in [4], [5], [23]. Such materials are described by their experimentally measured real permittivity and total loss tangent [36]. Biological samples on the other hand are electrically conductive with a significant contribution as they contain water. In that case, the power loss density reduces to Eq. (17).

$$p_{\text{samp}} = \frac{1}{2}\sigma|\overrightarrow{\mathrm{E}}|^2 \tag{17}$$

Noise (loss) involved in the signal acquisition during MRM experiments comes from the resistance of the dielectric ring resonator and from the conductive sample placed within the ring. As evoked in section II, the $\text{TE}_{01\delta}$ eigenmode of the ring resonator is very similar to that of the corresponding disk resonator (no hole). Therefore, in order to provide analytical expressions for the dielectric losses in each subvolume, the following approximations are used:

1) Losses in the dielectric resonator are small enough not to influence the field distribution. Therefore, the EM field expression used for computing dielectric losses is that of a lossless resonator.
2) The electric field distribution of the ring resonator

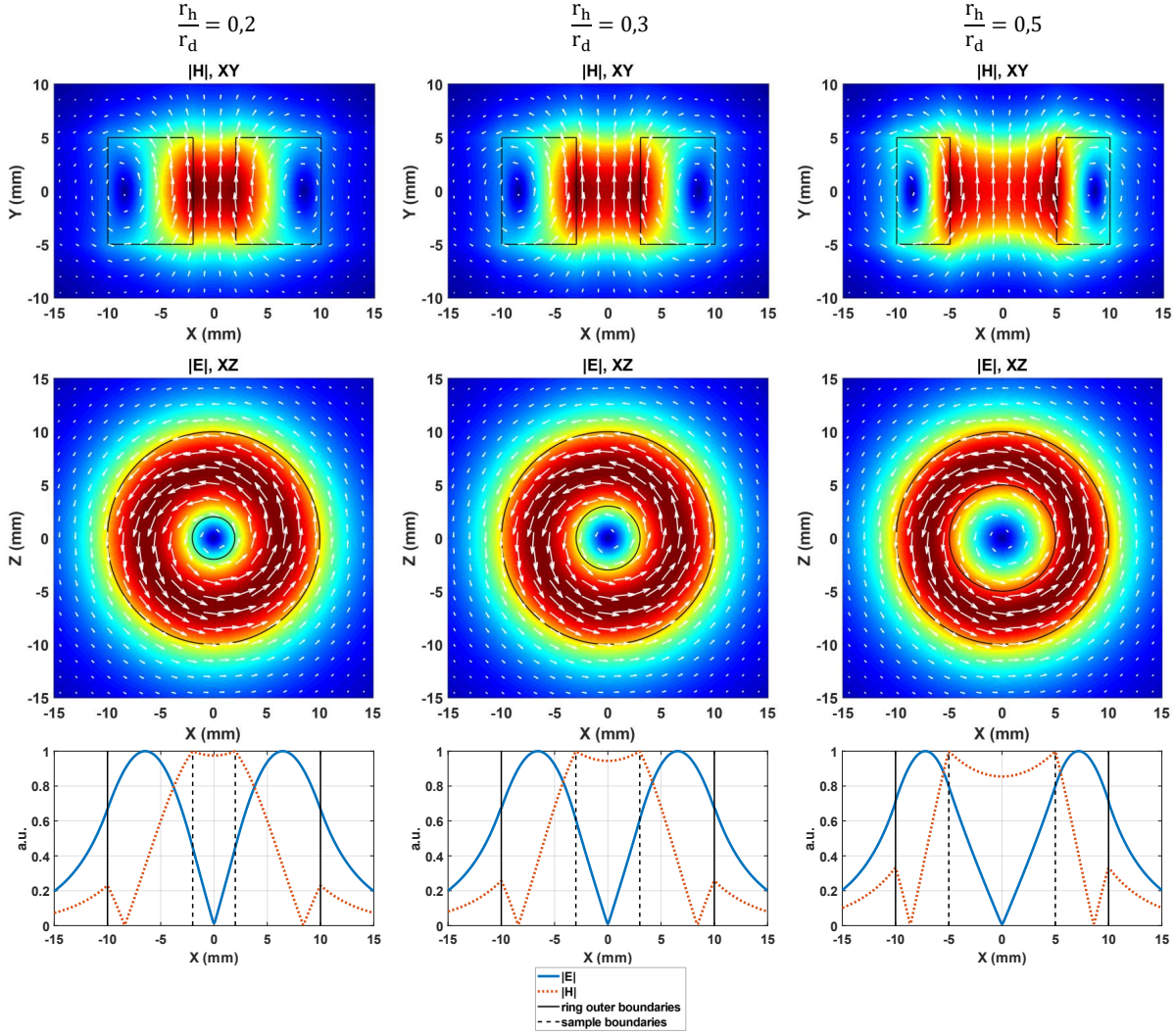

Figure 7. Normalized field maps for a dielectric ring (permittivity 500, height 10 mm, outer diameter 20 mm) filled with a sample of permittivity 50 for different inner to outer radii ratios. Top line: modulus of the total magnetic field. Middle line: modulus of the total electric field. Bottom line: field lines of the total electric (blue solid line) and magnetic (orange dotted line) fields in the center of the resonator ($y = 0$). The maps and field lines are normalized to the maximum value of the field modulus. Linear color scale from 0 to 1.

- is assumed equal to that of the disk resonator $\left(\overrightarrow{\mathrm{E}}^{\mathrm{disk}}(\mathbf{r})\right)$;
- and the field leakages through lateral boundaries can be neglected. As a result, the radial wavenumber α is quantified as x_{01}/r_{d} where x_{01} is the first zero of the zero-th order Bessel function of the first kind: $\mathrm{J}_0(x_{01}) = 0$.

3) The magnetic field decrease within the sample is due to its relative permittivity being different from that of the ring and quantified by the so-called penalty coefficient $\tau = \mathrm{H}_0^{\mathrm{sample}}/\mathrm{H}_0^{\mathrm{disk}}$ with $\mathrm{H}_0 = |\overrightarrow{\mathrm{H}}(\rho = 0, z = 0)|$. The field decrease, and the way the coefficient is estimated, are illustrated in Fig. 9. Its maximum value is 1, that corresponds to the disk ($\Delta\epsilon_{\mathrm{r}} = 0$) and it decreases toward zero with the increasing permittivity contrast. In practice, τ is estimated from the semi-analytically computed distributions considering field leakages at the boundaries, by comparing the H_0 value in the disk and in the sample excited by the ring resonator, with a correcting factor applied to ensure the following condition: $|\overrightarrow{\mathrm{H}}^{\mathrm{ring}}(\rho = r_{\mathrm{h}}, z = 0)| = |\overrightarrow{\mathrm{H}}^{\mathrm{disk}}(\rho = r_{\mathrm{h}}, z = 0)|$.

The two contributions for losses are therefore expressed as following.

Ring resonator losses:

$$\mathrm{P}_{\mathrm{loss}}^{\mathrm{ring}} = \frac{1}{2}\epsilon_0\epsilon_{\mathrm{r}}\omega\tan\delta\int_{V_{\mathrm{ring}}}|\overrightarrow{\mathrm{E}}^{\mathrm{disk}}(\mathbf{r})|^2\mathrm{d}^3\mathbf{r} \tag{18}$$

$$\mathrm{P}_{\mathrm{loss}}^{\mathrm{ring}} = \Delta\epsilon_0\epsilon_{\mathrm{r}}\omega\tan\delta\mathrm{L}_{\mathrm{eff}}\left(\mathrm{H}_0^{\mathrm{disk}}\right)^2\int_{r_{\mathrm{h}}}^{r_{\mathrm{d}}}\rho\mathrm{J}_1^2(\alpha\rho)\,\mathrm{d}\rho \tag{19}$$

$$\Delta = 2\pi\left(\frac{\omega\mu_0}{2\alpha}\right)^2 \tag{20}$$

$$\mathrm{L}_{\mathrm{eff}} = \left(1 + \frac{\sin(\beta\mathrm{L})}{\beta\mathrm{L}}\right)\mathrm{L} \tag{21}$$

$$\mathrm{P}_{\mathrm{loss,norm}}^{\mathrm{ring}} = \Delta\epsilon_0\epsilon_{\mathrm{r}}\omega\tan\delta\mathrm{L}_{\mathrm{eff}}\int_{r_{\mathrm{h}}}^{r_{\mathrm{d}}}\rho\mathrm{J}_1^2(\alpha\rho)\,\mathrm{d}\rho \tag{22}$$

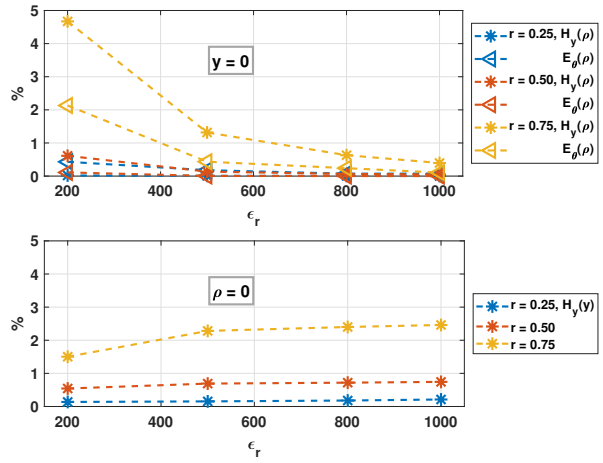

Figure 8. Error on the field distribution within the sample depending on the relative permittivity ϵ_r of the probe dielectric material, for 3 values of ratio $r = r_\mathrm{h}/r_\mathrm{d}$

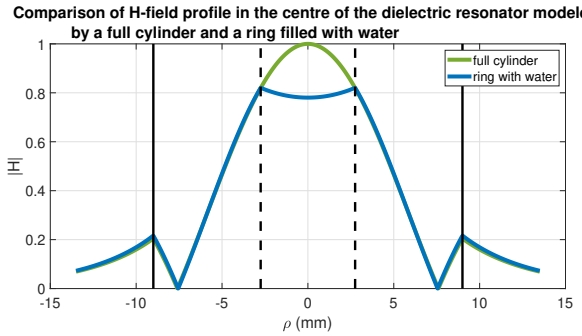

Figure 9. H-field (absolute value of the total field) decrease in water (semi-analytical method). Full (respectively dashed) lines indicate the outer (resp. inner) boundaries of the ceramic probe. The penalty factor τ defined in III is here estimated by the value of the blue curve in ρ = 0.

Sample losses:

$$\begin{aligned}\mathrm{P}_\mathrm{loss}^\mathrm{sample} &= \frac{1}{2}\sigma_\mathrm{sample}\tau^2\int_{V_\mathrm{samp}}|\overrightarrow{\mathrm{E}}^\mathrm{disk}(\mathbf{r})|^2\mathrm{d}^3\mathbf{r}\\ &= \Delta\sigma_\mathrm{sample}\mathrm{L}_\mathrm{eff}\left(\tau\mathrm{H}_0^\mathrm{disk}\right)^2\int_0^{r_\mathrm{h}}\rho\mathrm{J}_1^2(\alpha\rho)\,\mathrm{d}\rho\end{aligned} \tag{23}$$

$$\mathrm{P}_\mathrm{loss,norm}^\mathrm{sample} = \Delta\sigma_\mathrm{sample}\mathrm{L}_\mathrm{eff}\int_0^{r_h}\rho\mathrm{J}_1^2(\alpha\rho)\,\mathrm{d}\rho \tag{24}$$

To fully develop these expressions for dielectric losses, the integrals of the square of the first kind, first order Bessel function J_1 are derived from Eq. (25) from [37] generalized to arbitrary boundaries in Eq. (26).

$$\forall u \in R,$$
$$\int_0^u \rho\mathrm{J}_1^2(\alpha\rho)\,\mathrm{d}\rho = \frac{u^2}{2}\left[\mathrm{J}_1^2(\alpha u) - \mathrm{J}_0(\alpha u)\,\mathrm{J}_2(\alpha u)\right] \tag{25}$$

$$\begin{aligned}&\forall (u,v) \in R^2,\\ &\int_v^u \rho\mathrm{J}_1^2(\alpha\rho)\,\mathrm{d}\rho = \frac{u^2}{2}\left[\mathrm{J}_1^2(\alpha u) - \mathrm{J}_0(\alpha u)\,\mathrm{J}_2(\alpha u)\right]\\ &\qquad - \frac{v^2}{2}\left[\mathrm{J}_1^2(\alpha v) - \mathrm{J}_0(\alpha v)\,\mathrm{J}_2(\alpha v)\right]\end{aligned} \tag{26}$$

The model developed for the dielectric losses estimation was compared to numerical simulations performed with the CST Microwave Studio Eigenmode solver, which ignores material losses. In particular, a comparison was performed on the penalty factor τ and the normalized power losses term $\tau^2\mathrm{P}_\mathrm{loss,norm}^\mathrm{sample} + \mathrm{P}_\mathrm{loss,norm}^\mathrm{ring}$ in the case of a dielectric ring of permittivity 500, height 10 mm and outer diameter 20 mm; the ceramic loss tangent was 10^{-3}.

Regarding the validation of the penalty factor estimation, the sample permittivity varied between 1 and 100 and the inner over outer diameters ratio r = $r_\mathrm{h}/r_\mathrm{d}$ was 0.2, 0.3 and 0.5; while the normalized power losses were studied for ratio equal to 0.3 for varying sample properties (permittivity and conductivity). The penalty factor τ quantifies the decrease of H-field in the center of the sample, due to permittivity contrast between the ceramic material and the sample medium. As illustrated on Fig. 10, the lower the sample permittivity, the lower the penalty factor and the H-field magnitude. The magnetic field also decreases when increasing the sample diameter, that is the r ratio, and so does the error on the penalty factor estimation, which is otherwise barely affected by the sample permittivity value. For the three r ratio values considered here 0.2, 0.3 and 0.5, the maximum relative errors between the semi-analytical method and the full-wave simulations are 2.4%, 5.6% and 15.8%, respectively. In the last case, the model fails to describe properly the H-field distribution. The reason for this is that, as can be observed in Fig. 7, the E-field can no longer be assumed to be zero in the sample as its diameter increases. In consequence, we consider that the model should not be used for a diameter ratio higher than 0.5.

Fig. 11 represents the relative error between normalized total power losses from the developed model for the field distribution and the Eigenmode solver. The error is less than 5.1% in all the configurations considered here, that already cover a wide range of biological samples.

IV. Signal-to-Noise Ratio Estimation

The Signal-to-Noise Ratio (SNR) factor, defined in Eq. (27), can be expressed in terms of $\mathrm{H}_0^\mathrm{probe}$, the magnetic field in the sample,and $\mathrm{P}_\mathrm{loss}^\mathrm{probe}$, the total dielectric losses (from probe and sample). This quantity u_SNR (Eq. (27)) is useful not only in designing a ceramic probe with optimal parameters, but also to compare this probe performance to other MRM coil types, for example the commonly-used solenoid. u_SNR is equivalent, ignoring a multiplication factor of $\sqrt{2}$, to the resonator efficiency used by Mett et al. in their lumped-elements quivalent circuit approach [21], [22].

$$u_\mathrm{SNR}^\mathrm{probe} = \frac{\mathrm{H}_0^\mathrm{probe}}{\sqrt{\mathrm{P}_\mathrm{loss}^\mathrm{probe}}} \tag{27}$$

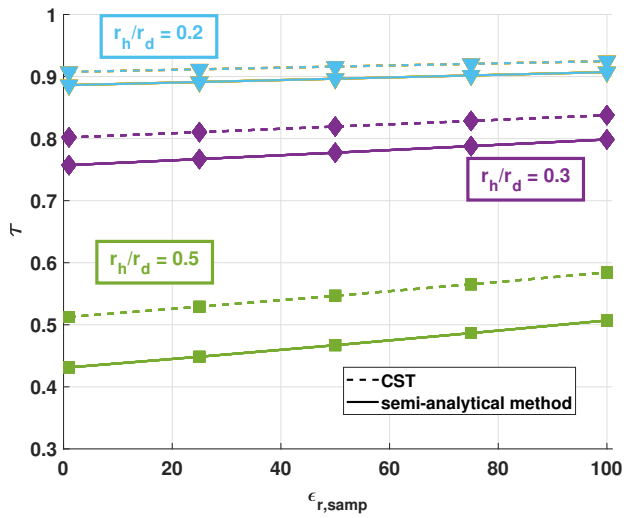

Figure 10. Comparison of the value of the penalty factor estimated with the developed field distribution model, to the value from numerical simulations, as a function of the sample permittivity.

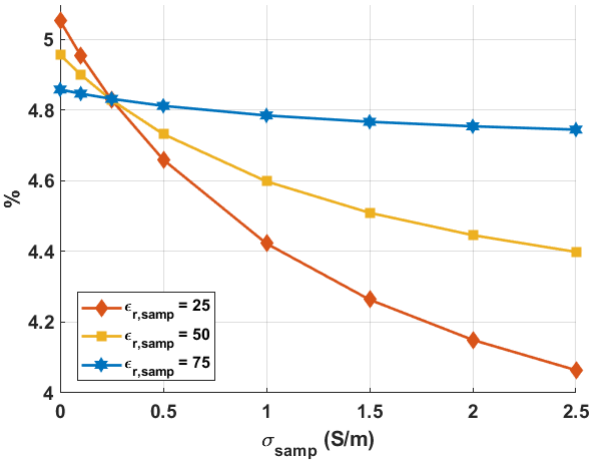

Figure 11. Comparison of semi-analytical model and numerical simulations results in terms of normalized power losses term $\tau^2 \mathrm{P}^{\mathrm{sample}}_{\mathrm{loss,norm}} + \mathrm{P}^{\mathrm{ring}}_{\mathrm{loss,norm}}$, as a function of the sample conductivity.

Considering the model hypothesis presented in III, the magnetic field within the sample is expressed as the product between the penalty factor τ and the H-field amplitude in the disk, H_0^{disk}. The power losses, accounting for electric field-sample interactions, are expressed by Eqs. (19) and (23). The H-field amplitude in the disk simplifies between numerator and denominator, and Eq.(27) becomes:

$$u^{\mathrm{DR}}_{\mathrm{SNR}} = \frac{\tau \mathrm{H}_0^{\mathrm{disk}}}{\sqrt{\mathrm{P}^{\mathrm{sample}}_{\mathrm{loss}} + \mathrm{P}^{\mathrm{ring}}_{\mathrm{loss}}}} = \frac{\tau}{\sqrt{\tau^2 \mathrm{P}^{\mathrm{sample}}_{\mathrm{loss,norm}} + \mathrm{P}^{\mathrm{ring}}_{\mathrm{loss,norm}}}} \quad (28)$$

The model proposed for the SNR factor estimation, herein after named SAM (Semi-Analytical Model) was applied to the case of a ceramic resonator prototype (outer diameter r_{d} = 18 mm, inner diameter r_{h} = 5.6 mm, height L = 10 mm, relative permittivity ϵ_{r} = 536, loss tangent tanδ = 8.10^{-4}) and was experimentally validated in [23]. In this paragraph, we compare the SNR factor provided by this probe, as a function of the sample conductivity, for two distinct values of sample relative permittivities, 50 and 81. Numerical simulations were performed using CST Microwave Studio, Frequency Domain Solver, with the dielectric ring resonator and a sample of diameter 4.5 mm and height 20 mm. In this configuration, the probe was fed through inductive coupling with a 3-mm loop placed at 3.8 mm from it , and is placed in the center of a metallic cylindrical shell representing the MR device bore (material: Perfect Electric Conductor, total length along z-axis: 600 mm, diameter: 91 mm). This is the most realistic case, compared to the simulations with the Eigenmode Solver in which no source is exciting the resonant mode. The SAM was also compared to a "combined method", in which the SNR factor is computed by estimating each variable in Eq. (27) with the discretized E-field (mesh step 0.2 mm) exported from the simulation software (Eigenmode solver). In particular, dielectric losses are derived by integrating the squared E-field multiplied by the local loss term (Eq. (16)) with the rectangle rule. Fig. 12 summarizes these results and Table I gives an example of numerical values for the computed parameters of Eq. (27).

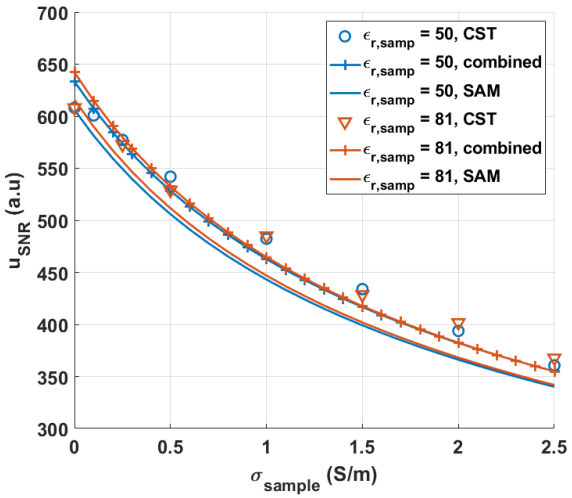

Figure 12. Comparison, in terms of SNR factor, of semi-analytical model (*SAM*) with numerical simulations results (Frequency domain solver of *CST* Microwave Studio) and Eq. (28) applied to the E-field distribution from the software Eigenmode solver (*combined*).

Table I
COMPUTED VARIABLES FOR A SAMPLE OF PERMITTIVITY 50 AND CONDUCTIVITY 1 S/M.

	SAM	Eigenmode solver
τ	0,77	0,81
$P_{loss,norm}$	0,30.10^{-5}	0,31.10^{-5}
u_{SNR}	445	463

For both permittivities, the CST, combined method and

SAM curves all follow the same decreasing trend when the sample conductivity is increased. The maximum relative error value between the semi-analytical and combined methods, and the realistic numerical simulations, was estimated at 8% and 5%, respectively. Both approaches produce results which are on the same order as errors intrinsic to experimental measurements of SNR in MRM, and these results also validate the approximations from Section III.

In the framework of the development of a Magnetic Resonance Microscopy probe, comparison of the SNR reachable by the dielectric probe with the conventional probe designs is of great interest in order to maximize the achievable SNR. In the case of the proposed sample and MR system described in Section I, the reference volume probe is the solenoid probe, and the SNR factor can be expressed following the guidelines described in [38], [12]. An example of such comparative study can be found in [23].

V. Discussion

The theoretical tools presented in this paper aim at assisting the design of dielectric probes for MRI. In this framework, the proposed approach is a simplified modeling of such resonator that enables to estimate its first TE mode frequency and the expected SNR factor, without relying on numerical simulations on initial examination. As presented in the previous sections II to IV, the accuracy of this method is satisfying for designing an optimized first prototype of such probe and was tested for realistic values of ceramic material permittivities [36] and usual values of biological samples permittivities (1 - 100) in the magnetic resonance imaging frequency range (from 100 MHz to 1 GHz). However, another aspect that was not undertaken previously is the computation time. Table II illustrates this point for the probe developed in [23], and for two different samples. The provided delays are averaged over 10 trials for each computed variable (frequency and SNR factor) and for each method. The margin of error is not provided if it is strictly sub-second. The computation is performed on a computer with 64 Go of RAM and an Intel Xeon processor (CPU E5-1630 v4). Regarding the SNR factor estimation with the Frequency domain solver of CST Studio (frequency range 700 - 780 MHz, tetrahedral mesh), the effective estimation delay is the given value, corresponding to the solver time, plus the time to tune and match the feeding loop at the desired Larmor frequency. From these results, there is no doubt that the theoretical approach is much faster than the numerical simulations.

VI. Conclusion

In summary, this paper addresses the topic of ceramic probes developed for Magnetic Resonance Microscopy. In particular, it proposes a semi-analytical model, based on the study of the first transverse electric mode of a high-permittivity dielectric ring, to estimate its resonance frequency and a measure of the SNR for evaluating the imaging performance of such probe. The knowledge of this quantity enables the comparison with standard probe configurations and can be used as design guideline to optimize the dielectric ring electromagnetic and geometrical properties.

Acknowledgment

This project has received funding from the European Union's Horizon 2020 research and innovation programme under grant agreement No 736937 (MCube project). Numerical simulations were supported by the Russian Foundation for Basic Research (grant No. 18-32-20115). Stanislav B. Glybovski was supported by the President of the Russian Federation (MK-3620.2019.8). Andrew G. Webb was partially supported by a H2020 European Research Council (ERC) Advanced Grant (NOMA-MRI 670629).

References

[1] L. Ciobanu, *Microscopic Magnetic Resonance Imaging: A Practical Perspective*. Pan Stanford, Singapore, 2017, ch. 2 and 7.

[2] H. Chen and R. Tycko, "Low-temperature magnetic resonance imaging with 2.8 μm isotropic resolution," *Journal of Magnetic Resonance*, vol. 287, pp. 47 – 55, 2018. [Online]. Available: http://www.sciencedirect.com/science/article/pii/S1090780717303087

[3] A. Webb, "Dielectric materials in magnetic resonance," *Concepts in magnetic resonance part A*, vol. 38, no. 4, pp. 148–184, 2011.

[4] K. Haines, T. Neuberger, M. Lanagan, E. Semouchkina, and A. Webb, "High Q calcium titanate cylindrical dielectric resonators for magnetic resonance microimaging," *Journal of Magnetic Resonance*, vol. 200, no. 2, pp. 349–353, 2009.

[5] T. Neuberger, V. Tyagi, E. Semouchkina, M. Lanagan, A. Baker, K. Haines, and A. Webb, "Design of a ceramic dielectric resonator for NMR microimaging at 14.1 Tesla," *Concepts in Magnetic Resonance Part B: Magnetic Resonance Engineering: An Educational Journal*, vol. 33, no. 2, pp. 109–114, 2008.

[6] D. Kajfez and P. Guillon, *Dielectric Resonators*. Noble Publishing Corporation, 1998, ch. 3.5, 1, 4, 4.4, pp. 90, 3, 185, 113, 128.

[7] Leung, Kwok Wa and Lim, Eng Hock and Fang, Xiao Sheng, "Dielectric resonator antennas: From the basic to the aesthetic," *Proceedings of the IEEE*, vol. 100, no. 7, pp. 2181–2193, 2012.

[8] Long, S and McAllister, Mark and Shen, Liang, "The resonant cylindrical dielectric cavity antenna," *IEEE Transactions on Antennas and Propagation*, vol. 31, no. 3, pp. 406–412, 1983.

[9] S. Fiedziuszko, "Dual-mode dielectric resonator loaded cavity filters," *IEEE Transactions on Microwave Theory and Techniques*, vol. 30, no. 9, pp. 1311–1316, 1982.

[10] Liang, Xiao-Peng and Zaki, Kawthar A, "Modeling of cylindrical dielectric resonators in rectangular waveguides and cavities," *IEEE transactions on microwave theory and techniques*, vol. 41, no. 12, pp. 2174–2181, 1993.

[11] Chen, S-W and Zaki, Kawthar A, "Dielectric ring resonators loaded in waveguide and on substrate," *IEEE transactions on microwave theory and techniques*, vol. 39, no. 12, pp. 2069–2076, 1991.

[12] K.R. Minard and R.A. Wind, "Solenoidal microcoil design—Part II: Optimizing winding parameters for maximum signal-to-noise performance," *Concepts in Magnetic Resonance*, vol. 13, no. 3, pp. 190–210, 2001.

[13] D.I. Hoult and R.E. Richards, "The signal-to-noise ratio of the nuclear magnetic resonance experiment," *Journal of Magnetic Resonance (1969)*, vol. 24, no. 1, pp. 71–85, 1976.

[14] D. Kajfez, A.W. Glisson, and J. James, "Computed modal field distributions for isolated dielectric resonators," *IEEE transactions on Microwave Theory and Techniques*, vol. 32, no. 12, pp. 1609–1616, 1984.

[15] J. Van Bladel, "On the resonances of a dielectric resonator of very high permittivity," *IEEE Transactions on Microwave Theory and Techniques*, vol. 23, no. 2, pp. 199–208, 1975.

[16] R. De Smedt, "Correction due to a finite permittivity for a ring resonator in free space," *IEEE transactions on microwave theory and techniques*, vol. 32, no. 10, pp. 1288–1293, 1984.

[17] M. Verplanken and J. Van Bladel, "The magnetic-dipole resonances of ring resonators of very high permittivity," *IEEE Transactions on Microwave Theory and Techniques*, vol. 27, no. 4, pp. 328–333, 1979.

[18] Yee, Hung Yuet, "Natural resonant frequencies of microwave dielectric resonators (correspondence)," *IEEE Transactions on Microwave Theory and Techniques*, vol. 13, no. 2, pp. 256–256, 1965.

[19] S.B. Cohn, "Microwave bandpass filters containing high-Q dielectric resonators," *IEEE Transactions on Microwave Theory and Techniques*, vol. 16, no. 4, pp. 218–227, 1968.

Table II
COMPARISON OF COMPUTATION TIMES IN THE CASE OF THE DIELECTRIC PROBE PRESENTED IN [23].

		Frequency		u_{SNR}	
$\epsilon_{\text{r,samp}}$	σ_{samp}	SAM	Eigenmode solver	SAM	Frequency domain solver
50	1 S/m	4 ms	4 min 31 s $\pm$ 2 s	7 s	1 min 29 $\pm$ 2 s
81	1,5 S/m	4 ms	4 min 28 s $\pm$ 5 s	7 s	1 min 32 s $\pm$ 1 s

[20] T. Itoh, and R.S. Rudokas, "New method for computing the resonant frequencies of dielectric resonators (short papers)," *IEEE Transactions on Microwave Theory and Techniques*, vol. 25, no. 1, pp. 52–54, 1977.

[21] R. R. Mett, J. W. Sidabras, I. S. Golovina, and J. S. Hyde, "Dielectric microwave resonators in TE 011 cavities for electron paramagnetic resonance spectroscopy," *Review of scientific instruments*, vol. 79, no. 9, p. 094702, 2008.

[22] R.R. Mett, J.W. Sidabras, J.R. Anderson, C.S. Klug, and J.S. Hyde, "Rutile dielectric loop-gap resonator for X-band EPR spectroscopy of small aqueous samples," *Journal of Magnetic Resonance*, vol. 307, p. 106585, 2019.

[23] M. A. C. Moussu, L. Ciobanu, S. Kurdjumov, E. Nenasheva, B. Djemai, M. Dubois, A. G. Webb, S. Enoch, P. Belov, R. Abdeddaim, and S. Glybovski, "Systematic analysis of the improvements in magnetic resonance microscopy with ferroelectric composite ceramics," *Advanced Materials*, vol. 31, no. 30, p. 1900912, 2019.

[24] S. J. Orfanidis, *Electromagnetic waves and antennas*. Sophocles J. Orfanidis, online, 2003, ch. 7.4, 1.14, pp. 289, 23–25. [Online]. Available: http://eceweb1.rutgers.edu/~orfanidi/ewa

[25] K. Zhang, D. Li, K. Chang, K. Zhang, and D. Li, *Electromagnetic Theory for Microwaves and Optoelectronics, Second Edition*. Springer, 2008, ch. 6.2, 6.8 and C.4, pp. 327–333, 387–394 and 685.

[26] R. K. Mongia and P. Bhartia, "Dielectric resonator antennas—a review and general design relations for resonant frequency and bandwidth," *International Journal of Microwave and Millimeter-Wave Computer-Aided Engineering*, vol. 4, no. 3, pp. 230–247, 1994.

[27] D. M. Pozar, *Microwave Engineering, Fourth Edition*. John Wiley & Sons, 2012.

[28] A. Kishk, A. Glisson, and G. Junker, "Bandwidth enhancement for split cylindrical dielectric resonator antennas," *Progress In Electromagnetics Research*, vol. 33, pp. 97–118, 2001.

[29] M. Rotaru and J. Sykulski, "Numerical investigation on compact multimode dielectric resonator antennas of very high permittivity," *IET science, measurement & technology*, vol. 3, no. 3, pp. 217–228, 2009.

[30] Y. Garault and P. Guillon, "Higher accuracy for the resonance frequencies of dielectric resonators," *Electronics Letters*, vol. 12, no. 18, pp. 475–476, 1976.

[31] R. F. Harrington, *Time-harmonic electromagnetic fields*. McGraw-Hill, 1961, ch. 7-4, pp. 321–325.

[32] J. Sheen, "A dielectric resonator method of measuring dielectric properties of low loss materials in the microwave region," *Measurement Science and Technology*, vol. 19, no. 5, p. 055701, 2008.

[33] E. Snitzer, "Cylindrical dielectric waveguide modes," *JOSA*, vol. 51, no. 5, pp. 491–498, 1961.

[34] Y.V. Shestopalov, and E.A. Kuzmina, "On a Rigorous Proof of the Existence of Complex Waves in a Dielectric Waveguide of Circular Cross Section," *Progress In Electromagnetics Research*, vol. 82, pp. 137–164, 2018.

[35] R. Petit, *Ondes électromagnétiques en radioélectricité et en optique, 2nde édition*. Masson Paris, 1993, vol. 2, ch. IV.5, pp. 97–99.

[36] E. Nenasheva, N. Kartenko, I. Gaidamaka, O. Trubitsyna, S. Redozubov, A. Dedyk, and A. Kanareykin, "Low loss microwave ferroelectric ceramics for high power tunable devices," *Journal of the European Ceramic Society*, vol. 30, no. 2, pp. 395–400, 2010.

[37] F. Bowman, *Introduction to Bessel functions*. Courier Corporation, 2012, ch. VI, p. 101.

[38] K. R. Minard and R. A. Wind, "Solenoidal microcoil design. Part I: Optimizing rf homogeneity and coil dimensions," *Concepts in Magnetic Resonance*, vol. 13, no. 2, pp. 128–142, 2001.

Marine A.C. Moussu received the Engineering degree (M.Sc. equivalent) from the École Supérieure de Physique et de Chimie Industrielles de la Ville de Paris (ESPCI Paris), Paris, France, in 2017, the M.Sc. degree in acoustics from Aix-Marseille Université, Marseille, in 2017 and the international M.Sc. degree Europhotonics from Aix-Marseille Université, Marseille, in 2017. She is currently pursuing the Ph.D. degree with Multiwave Imaging, Marseille, France, and the Institut Fresnel, Aix-Marseille Université, Marseille, France. Her research interests include wave physics applied to imaging and focusing, electromagnetic modelling and inverse problems.

Redha Abdeddaim was born in Alger, Algeria, in 1979. He received the Ph.D. degrees in physics from Paris X University, Paris, France, in 2007. He is currently an Assistant Professor in Aix Marseille University. His current research interests include Metamaterial, antennas and MRI coil.

Marc Dubois received the PhD degree in condensed matter from Université Paris Diderot, Paris, France, in 2014. He is currently a postdoctoral researcher with the Center of Magnetic Resonance for Biology and Medecine and the Institut Fresnel in Marseille, France. His current research interests include metamaterials and electromagnetism for MRI applications.

Elodie Georget received the Engineering degree (M.Sc. equivalent) in 2011 from the National Institute of Applied Sciences (INSA) of Rennes-France, specializing in communication systems and networks, and the Ph.D degree in Physics from Aix Marseille University in the CNRS research laboratory Institut Fresnel, in 2014. She is experienced in the field of electromagnetism working on the development of experimental techniques like RF antennae for MRI, metrology and electromagnetic characterization of materials. Prior to Multiwave, she worked at CEA-Neurospin for 2 years to pushed the boundaries on ultra-high field MRI coils. She is currently the head of the subsidiary Multiwave Imaging, Marseille, France and within it, of the MRI technologies department.

Andrew Webb graduated from the University of Bristol with a bachelors degree in Chemistry in 1986 and obtained his PhD from the University of Cambridge in 1989. After a postdoc in the Department of Radiology at the University of Florida, he joined the faculty of the Department of Electrical and Computer Engineering at the University of Illinois Urbana-Champaign. He was appointed full professor in 2000, and worked for three years in the Department of Physics at the University of Wurzburg on a Humboldt Fellowship. In 2008 he was appointed to run the newly-formed C.J.Gorter Centre in the Department of Radiology at Leiden University Medical Center. His main research areas are RF design for high field MRI, and translation of new engineering concepts into the clinic supported by an ERC Advanced Grant. Recently his lab has moved into the area of sustainable open-source low field MRI for developing countries funded by the Simon Stevin Preis. In addition to over 300 peer-reviewed publications he has authored four academic text books on medical imaging and biomedical instrumentation. He is an Associate Editor for Magnetic Resonance in Medicine and on the editorial board of several other MR journals. In 2020 he will be President of the European Society of Magnetic Resonance in Medicine and Biology. Most meaningfully in 2010 he founded the Nadine Barrie Smith trust which supports four student fellowships per year for women in science and engineering.

Elizaveta A. Nenasheva graduated from ElectroTechnical University, St. Petersburg, Russia with MS in Physics in 1974, and obtained her Ph. D. degree in Physics from Giricond Research Institute in 1981. She was a chief of the Department of Microwave Ceramics in Giricond Research Institute of St. Petersburg and now she is a director of company Ceramics. Dr. Nenasheva is an internationally recognized expert in designing of low loss microwave ceramic and ferroelectrics. She has also been active in the area of "smart" materials development, and ceramic technology applications for advanced accelerators R& D. Dr. Nenasheva has published more than 140 papers and has been granted with 50 national and world patents in the field of microwave ceramic compositions and ferroelectric technology development. In 2006-2007 and 2010 Dr. Nenasheva was a Visiting Professor of the High Energy Physics (HEP) Division of Argonne National Laboratory (ANL) and took part in researches of more than 10 grants of Department of Energy of USA.

Pavel Belov (Member, IEEE) was born in the USSR in 1977. He received MSc degree (Hons.) in applied mathematics from ITMO University, St. Petersburg, Russia, in 2000. He defended two Ph.D. theses: one in optics at ITMO University, St. Petersburg, Russia in 2003 and the second one in radioengineering at the Helsinki University of Technology, Espoo, Finland in 2006. He is currently the Dean of Physics and Engineering Faculty and Head of Research Center of Nanophotonics and Metamaterials, ITMO University. His current research interests include metamaterials, plasmonics, electromagnetics, nanophotonics, antennas, and nanostructures.

Stanislav B. Glybovski was born in Syktyvkar, Russia, in 1987. He received the M.Sc. and the Ph.D. degrees in radiophysics from St. Petersburg State Polytechnic University, St. Petersburg, Russia, in 2010 and 2013, respectively. He is currently a Senior Researcher with the Department of Physics and Engineering, ITMO University, St. Petersburg. His current research interests include antennas and microwave devices, computational electromagnetics, metamaterials, and MRI.

Luisa Ciobanu received her doctorate in physics from the Ohio State University in 2002. She then went on to do post-doctoral training in the Department of Electrical and Computer Engineering at University of Illinois at Urbana Champaign. After her postdoc, she has held research appointments at the Beckman Institute, University of Illinois at Urbana-Champaign and Pfizer, Inc. (Michigan, Ann Arbor). In 2007, she joined NeuroSpin at CEA-Saclay, France, where she heads the NeuroPhysics team. Her primary research interests include MR microscopy and its application to neuroscience investigations as well as the development of novel functional MRI techniques for ultra-high magnetic field imaging.

Stefan Enoch obtained his Ph.D. degree in Physics from Aix-Marseille University in 1997. He became Assistant Professor with Aix-Marseille University in 1998 and joined the CNRS in 2001. He has been Director of the Institut Fresnel for height years. He is currently Senior Researcher with the CNRS and Deputy Vice President for Sciences and Technologies of Aix-Marseille Université. Dr Enoch's research combines fundamental and applied research. His research involves the theory, modelling and engineering of the interaction between waves and their environment. Though his main contributions are in optics and more recently in microwaves, he has also made significant contributions to mechanical waves in solids. His work in optics started with fundamental investigations of the properties of photonic crystals, and has since shifted to the properties of metamaterials and their applications. He is considered an internationally recognized researcher on theory and modeling for nanophotonics. He has published about 150 research articles in top ranked journals, and he has given more than 40 invited and plenary presentations at a variety of conferences. His publications have been cited over 10300 times and his h-index is 46 (source Google Scholar). He recently led the Future and Emerging Technologies (FET) Open M-CUBE project that aims to improve the resolution of MRI by generating ultra-high fields using metamaterial antennas. The grant has ten partners, including two Small to Medium Enterprises, and has a budget of €3.9M. Briefly, the quality of images of ultra-high field MRI scanners is limited by spatial inhomogeneities of the radio-frequency field. He has also initiated the Marseille Imaging Institute, which has been created in July 2019 and of which he is now director. The ambition of Marseille Imaging is to lead, coordinate the imaging forces and strengthen the training-research link on the site as well as the attractiveness and socio-economic development. His research has attracted extensive coverage in the general and more general media: he was interviewed on French television (TV) (TF1), French radio (Radio France, Europe 1, France Inter), and in magazines (Le Point, La Recherche, Libération, Le Figaro), as well as in Physics World, Underwater Times, and New Scientist. He is member of the editorial board of the Journal of Modern Optics and has been Associate Editor of Optics Express from 2004 to 2012. He has also contributed to many conferences including Metamaterial's 2017 (scientific and organization committees) and ETOPIM9 (co-convenor).He received the Bronze Medal of the CNRS in 2006 and Aix-Marseille Innovation Award (Researcher category) in 2019. He has been elected Fellow of the European Academy of Sciences in 2019 and Fellow Member of the Optical Society of America in 2020.